

Towards density measurements in a supersonic turbulent boundary layer

R. Baidya*, S. Scharnowski, C. J. Kähler

Institute of Fluid Mechanics and Aerodynamics, Universität der Bundeswehr München, 85577 Neubiberg, Germany.

*Corresponding author: rio.baidya@unibw.de

Keywords: Calibrated schlieren, Supersonic flow, Turbulent boundary layer

ABSTRACT

Quantitative mean density measurements using calibrated schlieren technique are demonstrated in a Mach 2 compressible turbulent boundary layer. A calibration procedure, where schlieren and particle image velocimetry measurements are conducted on a symmetric double wedge model, is utilised. By assuming that the shock and expansion fan generated by the double wedge model can be idealised, the density gradient field is calculated based on the measured velocity field. Thus, based on the calibration data, a linear relation from schlieren intensity to density gradient is constructed. Moreover, to resolve a large range of density gradients expected within the boundary layer, schlieren measurements with five different knife edge positions are performed and the results are stitched together. The combined density gradient and the integrated density profiles showed good agreement with the literature, and therefore the current technique may provide a promising avenue to measure the mean density fields in compressible boundary layer flows.

1. Introduction

When investigating compressible turbulent boundary layers, it has now become a standard practice to account for the density variations with the distance from the wall via a transformation to enable comparison against the better understood incompressible counterpart. In particular, multiple studies have demonstrated that below the hypersonic regime (Mach number below 5) the canonical compressible and incompressible cases exhibit good agreement for the mean and turbulent stress profiles following transformations proposed by van Driest (1951) and Morkovin (1962), respectively. Consequently, theories and lower-order models developed for incompressible flows can be extended to the compressible regime, greatly improving our understanding of boundary layer flows in these regimes (Spina et al., 1994).

Experimentally, a wide range of methods such as Prandtl tube, hot-wire anemometry and particle image velocimetry (PIV) have been developed and improved to measure velocity. On the other hand, changes in the flow density, ρ , can be determined through shadowgraphy or schlieren visualisation. With calibration, the schlieren measurements can be used to quantitatively determine

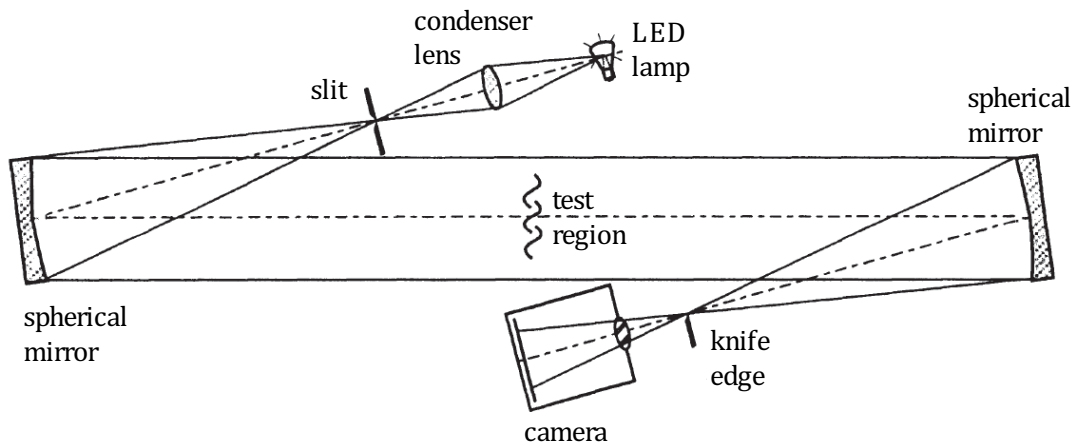


Figure 1. Schematic of a Z-type schlieren set-up used for the current study. Figure adapted from Settles (2001).

the density gradient field (Hargather & Settles, 2012). However, for compressible boundary layer flows, the large dynamic range of density and density gradient requires a careful adjustment of the schlieren sensitivity. Hence, the current work aims to analyse the possibility of measuring the density profile in the supersonic boundary layer by combining a range of schlieren settings to cover the large dynamic range present in the boundary layer, while still maintaining good sensitivity.

2. Experimental set-up

The experiments were conducted in the trisonic wind tunnel (TWM), located at the Bundeswehr University Munich. This is a blow-down type wind tunnel with a test section measuring 1800 mm × 300 mm × 675 mm along the length, width and height, respectively; and an operating Mach number ranging from 0.3 to 3.0 (Scharnowski et al., 2019).

A classical Z-type schlieren set-up as illustrated in figure 1 is used to record the schlieren intensity levels (Hampel, 1984). To ensure a high degree of parallelism is maintained between the light rays travelling through the test region, matching spherical concave mirrors with a focal length of 4 m are used. The slit and knife edge are located at the focal point of the mirrors and are oriented such that the variation in the schlieren image light intensity corresponds to the density gradient perpendicular to the streamwise direction. For the current work, the slit opening, $\mathcal{W}_{\text{slit}}$, is set to 2.25 mm while the knife edge can be adjusted in the direction perpendicular to the principal axis of the mirror (dash-dotted line in figure 1) to vary the deviation of light necessary in the test region to reach the knife edge. A Phantom v2640 camera was used to capture the schlieren images for the current study, but any monochrome camera with a good signal to noise ratio would have worked equally well.

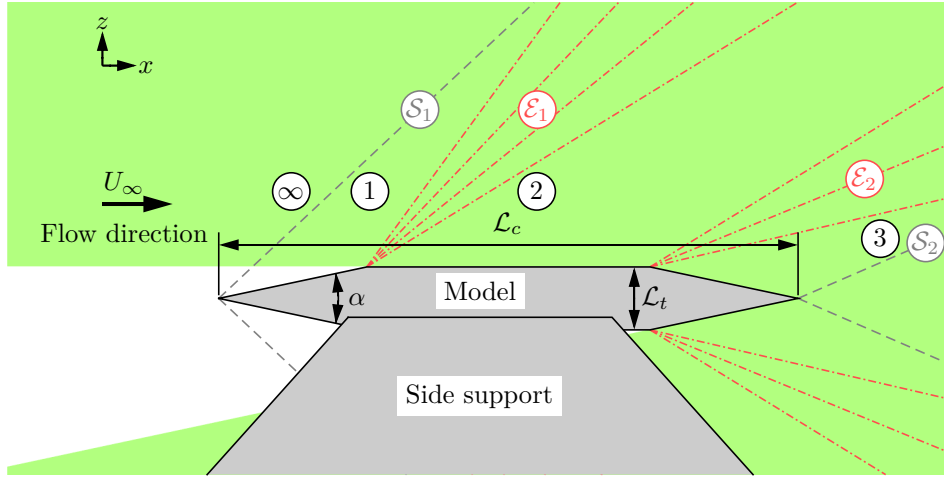


Figure 2. Schematic of set-up for schlieren calibration. \mathcal{L}_c , \mathcal{L}_t and α denote the chord, thickness and the wedge angle of the model, respectively. The shock (\mathcal{S}_1 and \mathcal{S}_2) and expansion (\mathcal{E}_1 and \mathcal{E}_2) locations, based on inviscid calculation, are indicated with the dashed and dash-dotted lines. The green shaded area shown corresponds to laser-illuminated region, for the PIV measurements.

M_∞	U_∞ (m s^{-1})	ρ_∞ (kg m^{-3})	$\sqrt{u^2/U_\infty^2}$ (%)	P_0 (kPa)	T_0 (K)
1.9	500	0.75	0.95	250	290

Table 1. Experiment parameters for the calibration measurements.

2.1. Schlieren calibration

A symmetric double wedge model, as shown in figure 2, is used to determine the relation between schlieren image intensity and density gradient. The model chord, thickness, and wedge angle are $\mathcal{L}_c = 180 \text{ mm}$, $\mathcal{L}_t = 20 \text{ mm}$ and $\alpha = 24^\circ$, respectively; while the angle of attack is set to zero. Note that, unlike in the schematic, the edges where the flat surfaces meet have a curvature with a radius of 0.5 mm in the actual model used for the experiments. The experimental condition for the calibration measurement is listed in table 1. Here, M_∞ , U_∞ and ρ_∞ correspond to the Mach number, velocity and density in the free stream, respectively. Moreover, P_0 and T_0 indicate the total pressure and total temperature in the settling chamber upstream of the Laval nozzle, while $\sqrt{u^2/U_\infty^2}$ denote the free-stream turbulence intensity levels.

Figure 3((a)–(d)) shows schlieren images for four different knife edge positions. The knife edge position, Δz_{ke} is defined with respect to the location where $\gamma = 0.5$, while the dark and bright regions in the images correspond to negative and positive density gradient with respect to the wall-normal direction, $d\rho/dz$. Here,

$$\Gamma = \frac{I - I_{\text{dark}}}{I_{\text{bright}} - I_{\text{dark}}} \quad (1)$$

corresponds to the normalised pixel intensity, where I , I_{dark} and I_{bright} correspond to the captured schlieren intensity, the dark image intensity where the knife edge fully blocks the focused light

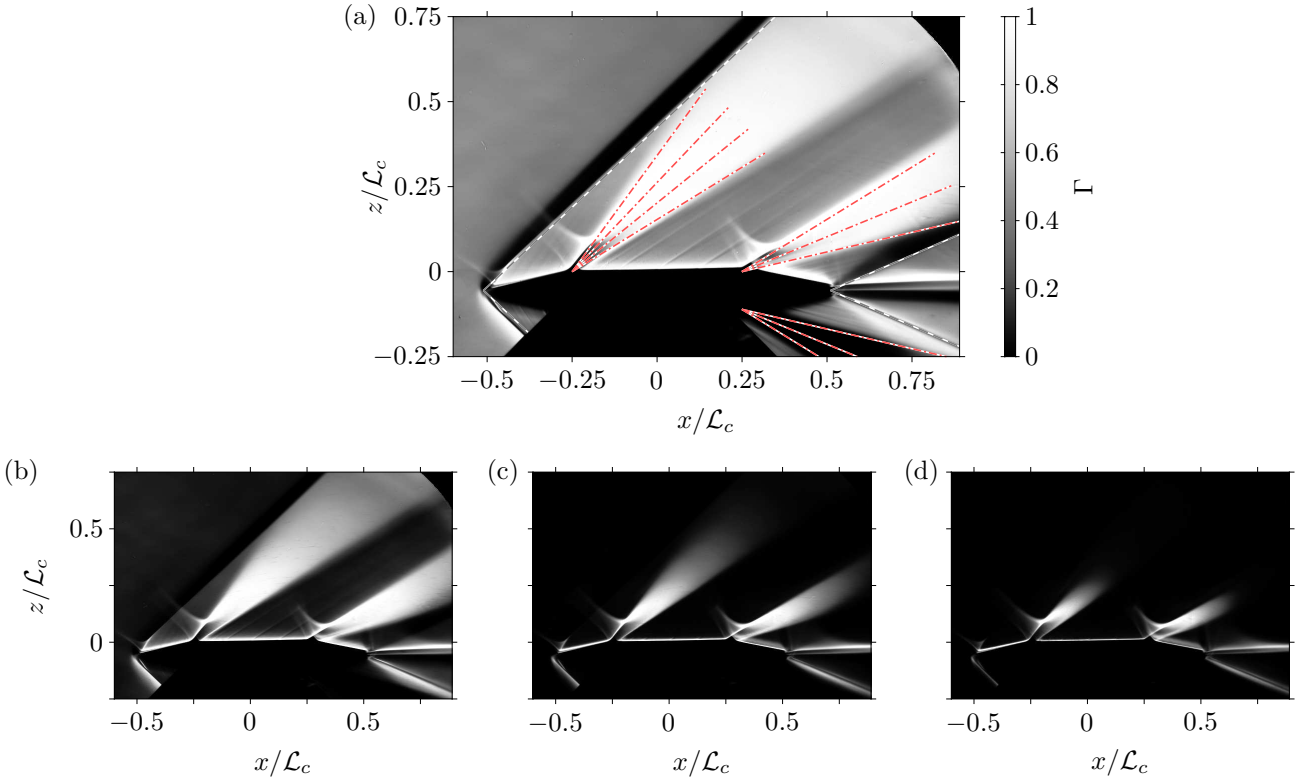


Figure 3. Schlieren images for different knife edge positions. (a–d) correspond to $\Delta z_{\text{ke}}/\mathcal{W}_{\text{slit}} = 0, -0.4, -1$ and -1.5 , respectively. The dashed and dash-dotted lines in (a) indicate the shock and expansion fan locations, respectively, according to the inviscid theory, as in figure 2.

and the bright image intensity where the knife edge allows all the focused light to pass through, respectively. Note that, to account for any non-uniformity in the lighting across the test region, I_{dark} and I_{bright} are determined for each pixel by temporally averaging 200 images taken over 10 s at a 20 Hz recording rate. In contrast, I is a temporal mean of 1000 images acquired at 1 kHz.

It is evident from figure 3(a), that a single knife edge position is not sufficient to resolve the full range of density gradient present in the flow as the images saturate beyond a critical $d\rho/dz$ range. Furthermore, by adjusting Δz_{ke} the critical range is translated, and by piecewise combining several knife edge positions the resolvable $d\rho/dz$ range can be greatly extended.

To determine the density gradient of the flow around the double wedge model, velocities across a similar field of view with schlieren images are measured using PIV as shown in figure 4(a). Furthermore, by assuming ideal shock and expansion fan, the density in the expansion fan region 1 and 2 (\mathcal{E}_1 and \mathcal{E}_2) can be calculated as (Elsinga et al., 2004)

$$\frac{\rho}{\rho_{2,\infty}} = \left[1 + \frac{\gamma - 1}{2} M_{2,\infty}^2 \left(1 - \frac{|\mathbf{U}|^2}{U_{2,\infty}^2} \right) \right]^{\frac{1}{\gamma-1}}, \quad (2)$$

where $\gamma = 1.4$ is the ratio of specific heats for air. Here, U and M denote the streamwise velocity and Mach number. Moreover, the subscript $2, \infty$ denotes values from the inviscid calculation for region 2 between the two expansion fans, while \mathbf{U} is the temporal-averaged velocity vector evalu-

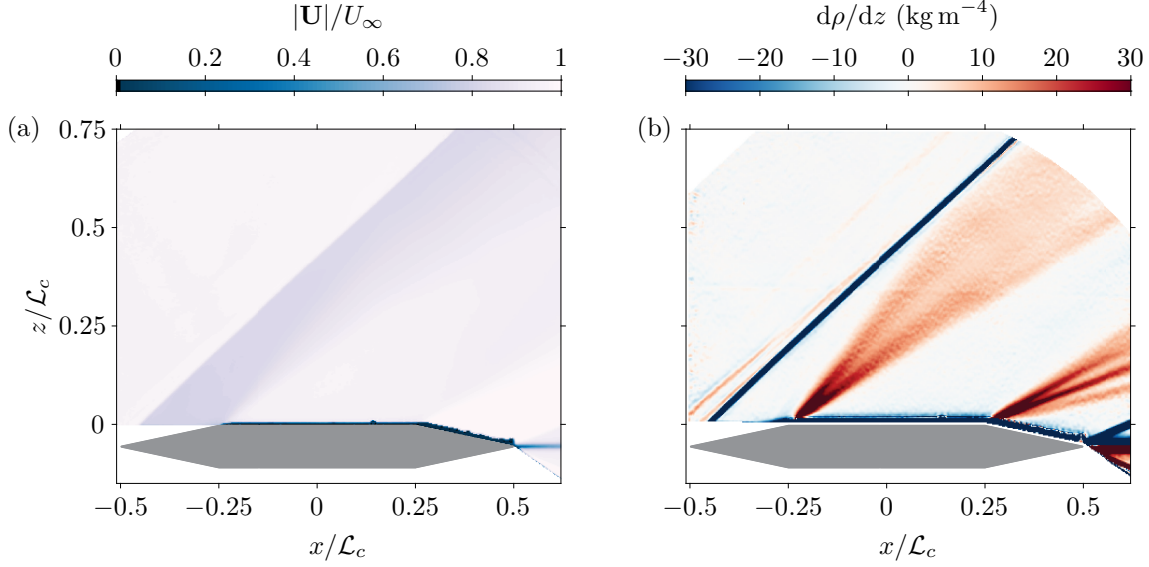


Figure 4. (a) Measured velocity magnitude field, (b) wall-normal density gradient field based on (a).

ated from the PIV measurements. The calculated density is then numerically differentiated using a least squares approach (Raffel et al., 2018) to obtain $\partial\rho/\partial z$ as shown in figure 4(b).

Despite accounting for non-uniformity in the lighting across the test region in eq. (1), it was observed that Γ is not always a constant across the field of view for a wind-off image with no flow. Therefore, here we propose that change in Γ between the wind-on and wind-off conditions and the density gradient follow a linear relation (Hargather & Settles, 2012). I.e.

$$d\rho/dz = a(\Gamma - \Gamma_{\text{wind-off}}) + b, \quad (3)$$

where Γ and $\Gamma_{\text{wind-off}}$ correspond to the normalised intensity for the wind-on and wind-off conditions for a given knife edge position, respectively; while a and b are coefficients determined using a robust linear fit.

To assess the validity of eq. (3), figure 5 shows the linear fit (dashed line) along with the joint probability distribution function (PDF) between the change in Γ and $d\rho/dz$. Note that, here the intensity level and density gradient are evaluated independently from schlieren and PIV measurements and the joint PDF is constructed by interpolating them to a common (x, z) Cartesian grid points. Furthermore, only the region in the vicinity of the first expansion (\mathcal{E}_1), where the approximations leading to eq. (2) is expected to hold best, is considered when calculating the joint PDF. Note that, for the $\Delta z_{\text{ke}}/\mathcal{W}_{\text{slit}} \approx -1.5$ case (figure 5b), the schlieren image is saturated at low Γ values (as indicated by vertically elongated dotted and dash-dotted contours) and therefore these regions are removed (and are shown clipped) before determining the linear relation. Figure 5 indicates that for a fixed $\Gamma - \Gamma_{\text{wind-off}}$, the distribution of $d\rho/dz$ is wide — leading to a substantial portion of the calibration data to deviate from the linear relationship and it may correspond to a bottleneck that limits the lower bound of achievable uncertainty using the current technique.

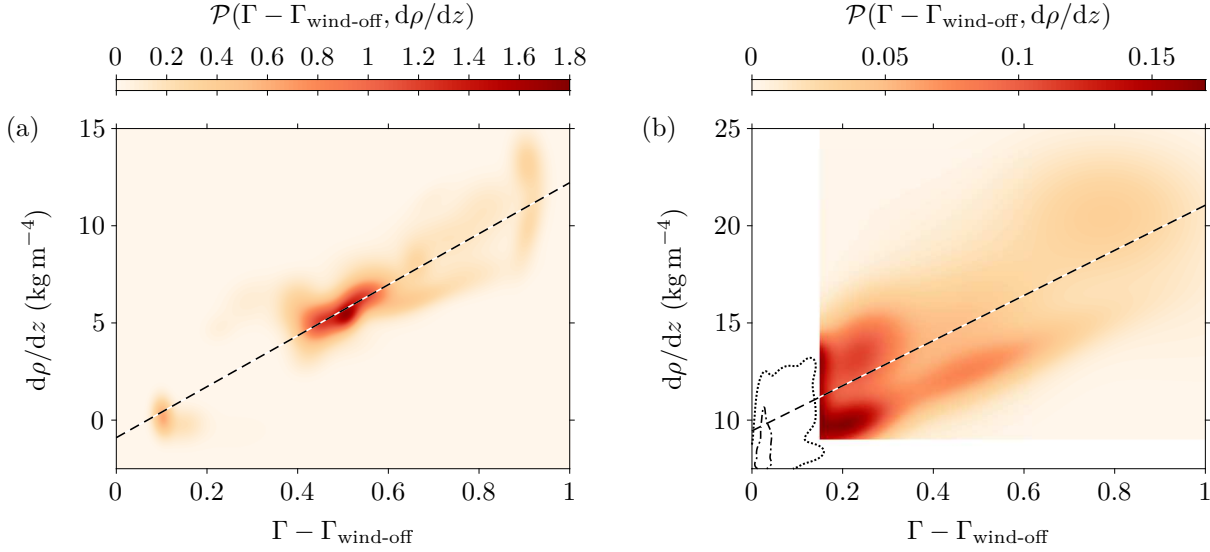


Figure 5. Joint PDF between normalised intensity and density gradient. (a) and (b) correspond to two different knife edge positions where $\Delta z_{\text{ke}}/\mathcal{W}_{\text{slit}} = -0.4$ and -1.5 , respectively. The dashed lines indicate the fitted relation between intensity and density gradient, while the dotted and dash-dotted lines in (b) are contour levels 0.2 and 2.

M_∞	U_∞ (m s^{-1})	ρ_∞ (kg m^{-3})	P_0 (kPa)	T_0 (K)	δ_{99} (m)	Re_τ
2.0	505	0.71	250	290	0.014	4500

Table 2. Experiment parameters for the boundary layer measurements. Note that, δ_{99} and Re_τ values have been estimated based on tabulated results from Bross et al. (2021).

2.2. Flat plate boundary layer

To measure the density profile in a canonical compressible boundary layer, the double wedge model is replaced with the flat plate model reported in Bross et al. (2021). PIV measurements on the flat plate have shown that the resulting boundary at a free-stream Mach number equal to 2.0 agrees well with the incompressible zero-pressure-gradient (ZPG) turbulent boundary layer (TBL) profile, once accounted for the variation in ρ within the boundary layer (Baidya et al., 2020). The schlieren measurements were performed at $x \approx 1.2$ m downstream from the leading edge of the 1.65 m long model with knife edge position at $\Delta z/\mathcal{W}_{\text{slit}} = 0, -0.4, -1$ and -1.5 as in calibration measurements and an additional measurement at $\Delta z/\mathcal{W}_{\text{slit}} = -2$. Furthermore, all measurements were recorded at 1 kHz for 1 second.

The experimental parameter for the boundary layer measurement is summarised in table 2. Here, δ_{99} corresponds to the boundary layer thickness and is equal to z location where the mean velocity is equal to $0.99U_\infty$. Moreover, $Re_\tau = \delta_{99}U_\tau/\nu_w$ is the friction based Reynolds number, where U_τ and ν_w denote the mean friction velocity and kinematic viscosity of fluid at the wall.

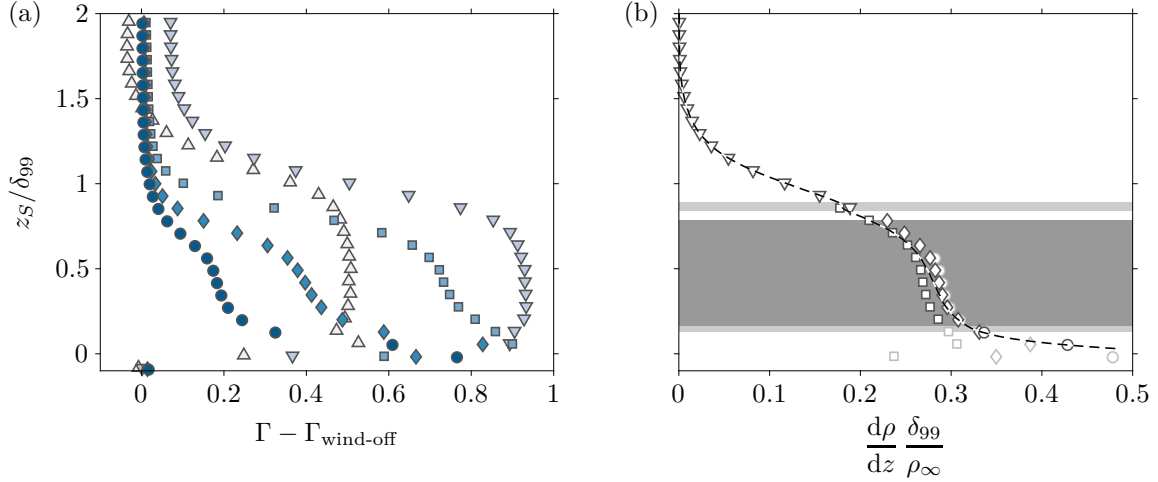


Figure 6. Calculated (a) normalised intensity and (b) wall-normal density gradient profiles. The symbols correspond to different knife edge positions and are shown filled with an increased shading for a stronger cut-off (more negative Δz_{ke}) in (a). (b) The dashed line is the combined profile, the grey shaded regions denote the overlap between the different knife edge positions, and the discarded sections of the individual profiles are shown in lighter shading.

3. Boundary layer profiles

Figure 6(a) shows the normalised intensity deviation from the wind-off condition for different knife edge positions. Note that, z_S in the ordinate corresponds to the wall-normal coordinate based on the camera sensor. It turns out that, due to the deflection of light as a result of density gradients present in the test region, the intensity level corresponding to a certain z location is displaced and recorded at z_S instead (a correction procedure to account for the light deflection is proposed in §3.2).

Figure 6(b) shows the transformed density profile for each knife edge position (only the sections where the linear relation between $\Gamma - \Gamma_{\text{wind-off}}$ and $d\rho/dz$ holds are shown). Note that, while the knife edge positions corresponding to $\Delta z_{\text{ke}} = 0, -0.4, -1$ and -1.5 are transformed based on the calibration measurements described in §2.1, the transformation for the $\Delta z_{\text{ke}} = -2$ case is determined based on the calculated $d\rho/dz$ from the $\Delta z_{\text{ke}} = -1.5$ case and the corresponding $\Gamma - \Gamma_{\text{wind-off}}$ from the boundary layer measurements, due to lack of calibration at this particular knife edge position. In other words, the $d\rho/dz$ profile for the $\Delta z_{\text{ke}} = -2$ case is matched to the $\Delta z_{\text{ke}} = -1.5$ case within $0.25 \leq z_S / \delta_{99} \leq 0.58$.

3.1. Combined profile

The piecewise profiles shown in figure 6(b) follow the expected behaviour where they transition between the different knife edge cases to within $\pm 2.5\%$ of the maximum measured $d\rho/dz$. Note that the $\Delta z_{\text{ke}} = 0$ case was omitted (and therefore not included in figure 6b) when stitching the piecewise profiles to create a combined overall profile. This was because unlike the $\Delta z_{\text{ke}} = -0.4$ case (∇ symbols), the profile for the $\Delta z_{\text{ke}} = 0$ case did not smoothly transition to $d\rho/dz = 0$ when $z > \delta_{99}$ as expected.

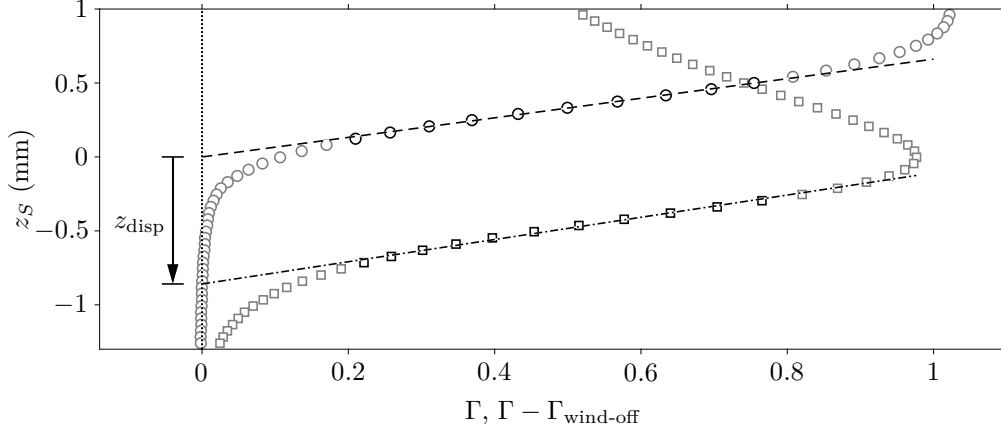


Figure 7. Schlieren intensity profile as function of the recorded z_S location, based on the camera sensor. The circle symbol shows the normalised intensity, Γ , for the wind-off, bright image ($\Delta z_{ke}/\mathcal{W}_{slit} \approx 1$). The squares correspond to the normalised intensity difference, $\Gamma - \Gamma_{\text{wind-off}}$, for the knife edge position $\Delta z_{ke}/\mathcal{W}_{slit} = -2$. The region used to determine the linear fit (dash and dash-dotted lines) are shown in darker shading.

The procedure to determine the overlap region between the piecewise profiles indicated by the shaded region in figure 6(b) is as following:

1. The longest continuous z_S location where the difference in $d\rho/dz$ profiles from two adjacent knife edge positions is less than 5% (1% in the case of $\Delta z_{ke} = -2$, since the profiles are matched for this case due to lack of corresponding calibration measurement) of the maximum $d\rho/dz$ is found.
2. If the overlap regions for more than two adjacent knife edge positions coincide, the overlap region that extends closest to the wall takes precedent except for the $\Delta z_{ke} = -2$ case, which has the lowest precedent. For the remaining overlap region, the z location is truncated so that the coincident section is removed.

The piecewise $d\rho/dz$ profiles are blended over the overlap region and stitched together to create an overall profile represented by the dashed line in figure 6(b). Furthermore, the symbols correspond to the piecewise profile from different knife edge positions, with light/dark shading denoting sections that were discarded/utilised to construct the combined profile.

3.2. Wall-normal correction procedure

As mentioned in §3, the z location recorded on the sensor is displaced from the true z location, due to deflection of light in the high density gradient region. Here, we assume that the displacement is proportion to the density gradient to construct a transformation from z_S to z . I.e.

$$z = z_S + \frac{z_{\text{disp}}}{d\rho/dz|_{\text{max}}} \frac{d\rho}{dz}, \quad (4)$$

where z_{disp} is the recorded wall position on the sensor. To determine the location of the wall for the wind-off and wind-on conditions, a linear fit for the normalised intensity is performed in the

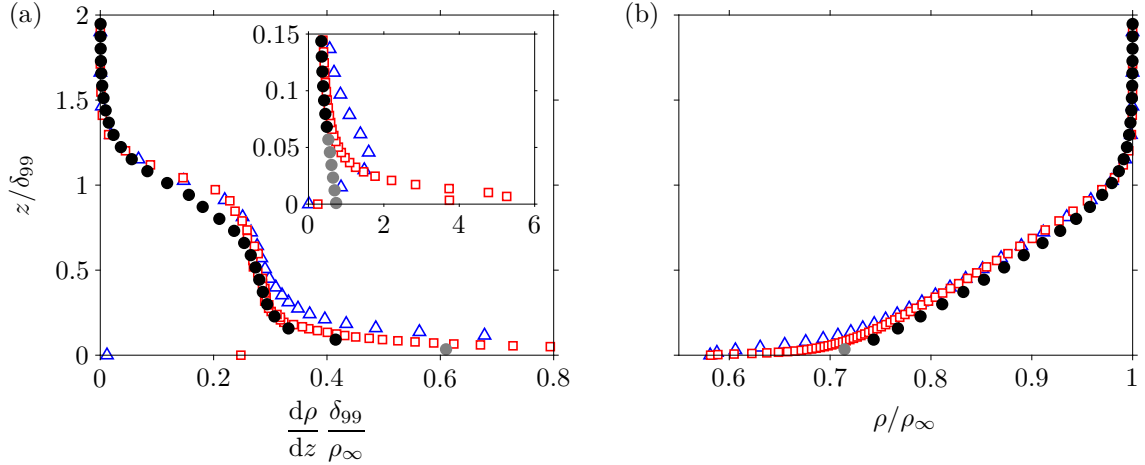


Figure 8. (a) Mean wall-normal density gradient ($d\rho/dz$) and (b) mean density (ρ) profiles in a Mach 2 ZPG TBL. The inset shows the full range of $d\rho/dz$ close to the wall. The black symbols correspond to the combined profile from four different knife edge positions, while the grey symbols denote the near-wall modelled profile. The empty symbols are from DNS at Mach 2, with blue and red indicating $Re_\tau = 200$ and 1110 cases, respectively (Pirozzoli & Bernardini, 2011). Note that, only selective wall-positions are shown here for easier distinction between the profiles.

near-wall region where Γ transitions from zero to a finite value. The linear fit is then extended to $\Gamma = 0$ and this intercept point for the wind-off condition with the knife edge position allowing all the focused light to pass through ($\Delta z_{ke}/\mathcal{W}_{slit} \approx 1$) is considered to be the origin of z_S . Similarly, the intercept point for the wind-on condition and knife edge position at $\Delta z_{ke}/\mathcal{W}_{slit} = -2$ is considered to be z_{disp} . For added clarity, the procedure is illustrated in figure 7.

When the maximum measured $d\rho/dz$ is compared against direct numerical simulation (DNS) results, it was found to be significantly smaller than the peak DNS values. The DNS suggests that the peak value can be an order of magnitude higher than the values encountered in the log region (see figure 8a), and extending the current approach to cover such a large range would be very challenging since a further reduction in the knife edge position would likely lead to significant reduction in signal to noise ratio. Thus, here we instead model the near-wall behaviour, where $d\rho/dz$ values are linearly extended to the wall below z location where $d^2\rho/dz^2$ is minimum ($d^2\rho/dz^2 < 0$ throughout the boundary layer, except in the close vicinity to the wall), based on the DNS. Thus,

$$\frac{d\rho}{dz_{\text{model}}} = \frac{d^2\rho}{dz^2} \Big|_{\text{min}} (z - z_M) + \frac{d\rho}{dz} \Big|_{z=z_M}, \quad (5)$$

where z_M corresponds to the z location where $d^2\rho/dz^2$ is minimum. Subsequently, $d\rho/dz|_{\text{max}}$ in eq. (4) can be replaced with $d\rho/dz_{\text{model}}|_{z=0}$. Thus, z is iteratively solved to satisfy eqs. (4) and (5) until the maximum change in z from the previous iteration correspond to a sub-pixel movement on the camera sensor.

3.3. Comparisons against the literature

Figure 8(a) shows the measured mean $d\rho/dz$ profile with corrected z position (solid symbol) against DNS profiles from Pirozzoli & Bernardini (2011) (empty symbols). While the modelled part of

the profile (grey coloured) is underestimated compare to DNS, the measured values in the region $z/\delta_{99} > 0.07$ (black coloured) are in good agreement with DNS. Note that, for consistency δ_{99} utilised for DNS has been reevaluated using the same procedure as the experiment (which was within 2 % of the reported value).

Finally, to obtain the mean density profile, $d\rho/dz$ is numerically integrated starting with the free-stream condition obtained from the inviscid calculation and marching towards the wall using the trapezoidal rule. The calculated ρ profile is compared with DNS results in figure 8(b). The measured values are in general smaller than that from DNS, however, this discrepancy could be due to the deficit in the wake region still approaching the asymptotic value, even 1.2 m downstream of the leading edge, as suggested by a shallower wake observed compared to the canonical incompressible profile measured more than 10 m downstream of a sandpaper trip (Baidya et al., 2020).

4. Summary and conclusions

Density measurements in a Mach 2 compressible boundary layer utilising a calibrated schlieren technique are presented. A calibration procedure, where schlieren and PIV measurements on a symmetric double wedge model are conducted, is used to determine the relation between schlieren image intensity and density gradient. By considering the shock and expansion fan generated by the double wedge model to be ideal, density gradient fields could be calculated from the PIV velocity fields. Thus, a linear relation between schlieren intensity and density gradient is constructed. We found that the density gradient from the calibration data has a wide distribution and that a substantial portion of the data deviates from the linear relation – a bottleneck that may limit the uncertainty of the current technique.

To cover a large range of density gradients present in a boundary layer, schlieren measurements were performed with five different knife edge positions. The piecewise density gradient profiles were then stitched together to create an overall profile. In addition to the working principle of schlieren that leads to an increased intensity for a stronger density gradient, the deflection of light in the high-density gradient region is also found to displace the recorded position of the light intensity on the camera sensor. To account for this displacement, we propose a first-order model as a function of the distance from the wall for the near-wall region which is not captured from the experiment. Then, the displacement is assumed to follow a linear relation with the density gradient to enable transformation from the recorded to the true wall-normal coordinate.

The mean density gradient and the integrated density profiles from the experiment, once corrected for the wall-normal displacement, showed good agreement with direct numerical simulation results at a matched Mach number and a similar Reynolds number. Thus, the current technique provides a promising avenue to measure the mean density fields within compressible turbulent boundary layer flows.

Acknowledgements

Funding for this work was provided by the German Research Foundation (Deutsche Forschungsgemeinschaft – DFG) through Research Grants under project no. 448354709, which is gratefully acknowledged.

References

- Baidya, R., Scharnowski, S., Bross, M., & Kähler, C. J. (2020). Interactions between a shock and turbulent features in a Mach 2 compressible boundary layer. *Journal of Fluid Mechanics*, 893.
- Bross, M., Scharnowski, S., & Kähler, C. J. (2021). Large-scale coherent structures in compressible turbulent boundary layers. *J. Fluid Mech.*, 911.
- Elsinga, G. E., Van Oudheusden, B. W., Scarano, F., & Watt, D. W. (2004). Assessment and application of quantitative schlieren methods: Calibrated color schlieren and background oriented schlieren. *Exp. Fluids*, 36(2), 309–325.
- Hampel, A. (1984). *Auslegung, Optimierung und Erprobung eines vollautomatisch arbeitenden Transsonik-Windkanals* (Unpublished doctoral dissertation). Hochschule der Bundeswehr.
- Hargather, M. J., & Settles, G. S. (2012). A comparison of three quantitative schlieren techniques. *Opt. Lasers Eng.*, 50(1), 8–17.
- Morkovin, M. V. (1962). Effects of compressibility on turbulent flows. *Mécanique de la Turbulence*, 367(380), 26.
- Pirozzoli, S., & Bernardini, M. (2011). Turbulence in supersonic boundary layers at moderate Reynolds number. *J. Fluid Mech.*, 688, 120–168.
- Raffel, M., Willert, C. E., Scarano, F., Kähler, C. J., Wereley, S. T., & Kompenhans, J. (2018). *Particle image velocimetry: A practical guide*. Springer.
- Scharnowski, S., Bross, M., & Kähler, C. J. (2019). Accurate turbulence level estimations using PIV/PTV. *Exp. Fluids*, 60(1), 1.
- Settles, G. S. (2001). *Schlieren and shadowgraph techniques: visualizing phenomena in transparent media*. Springer Science & Business Media.
- Spina, E. F., Smits, A. J., & Robinson, S. K. (1994). The physics of supersonic turbulent boundary layers. *Annu. Rev. Fluid Mech.*, 26(1), 287–319.
- van Driest, E. R. (1951). Turbulent boundary layer in compressible fluids. *J. Spacecr. Rockets*, 18(3), 145–160.